Journal of Zhejiang University-SCIENCE A 2025 26(10):950-966
www.jzus.zju.edu.cn; www.springer.com/journal/11582
E-mail: jzus_a@zju.edu.cn

Research Article
https://doi.org/10.1631/jzus.A2400341

Check for updates

Numerical study on the failure characteristics and reinforcement effects of shield segmental linings subjected to localized overload

Long ZHOU[1], Zhiguo YAN[2], Mengqi ZHU[2]✉

[1]*School of Safety Science and Engineering (School of Emergency Management), Nanjing University of Science and Technology, Nanjing 210094, China*
[2]*College of Civil Engineering, Tongji University, Shanghai 200092, China*

Abstract: When only a portion of the shield lining structures in a full-line tunnel are overloaded, their bearing and failure characteristics are significantly different from those in the full-line overloaded case. In existing studies, one or several segmental lining rings have been studied, with overload applied to selected lining rings to analyze the performance evolution of the lining structures; however, this approach fails to reveal the bearing and failure characteristics of shield lining rings under localized overload. To address this research gap, we employ 3D finite element modeling to investigate the mechanical performance and failure mechanisms of shield segmental linings under localized overload conditions, and compare the results with full-line overload scenarios. Additionally, the impact of reinforcing shield segmental linings with steel rings is studied to address issues arising from localized overloads. The results indicate that localized overloads lead to significant ring joint dislocation and higher stress on longitudinal bolts, potentially causing longitudinal bolt failure. Furthermore, the overall deformation of lining rings, segmental joint opening, and stress in circumferential bolts and steel bars is lower compared to full-line overloads. For the same overload level, the convergence deformation of the lining under full-line overload is 1.5 to 2.0 times higher than that under localized overload. For localized overload situations, a reinforcement scheme with steel rings spanning across two adjacent lining rings is more effective than installing steel rings within individual lining rings. This spanning ring reinforcement strategy not only enhances the structural rigidity of each ring, but also limits joint dislocation and reduces stress on longitudinal bolts, with the reduction in maximum ring joint dislocation ranging from 70% to 82% and the reduction in maximum longitudinal bolt stress ranging from 19% to 57% compared to reinforcement within rings.

Key words: Shield segmental lining; Localized overload; Failure characteristics; Steel ring reinforcement

1 Introduction

The shield tunneling technique has been extensively applied to construct highway, railway, and urban subway tunnels in soft soil strata. The approach is favored for its adaptability to challenging ground conditions and minimal impact on the surface environment (Hu et al., 2022; Elbady et al., 2023; Ran et al., 2023). For shield segmental linings assembled with precast reinforced concrete segments and bolts, there are many joints in the lining structures, and the existence of joints presents challenges in terms of stress and deformation of the lining structures (Kannangara et al., 2022; Lu et al., 2024; Wei et al., 2024). During the operational period, the changing of surrounding loads can cause excessive convergence deformation in shield lining structures, which can lead to issues such as joint opening and dislocation, water leakage, and cracking of concrete around the joints (Sharghi et al., 2023; Wang et al., 2023; Ye et al., 2024; Zheng et al., 2024). Therefore, many researchers have investigated the mechanical behavior of shield segmental linings in response to changes in surrounding loads.

For instance, Liu et al. (2016, 2017) conducted full-scale tests to analyze the bearing capacity and failure mechanisms of continuous-jointed and stagger-jointed segmental linings, with the results showing that segmental lining structures were more vulnerable to

✉ Mengqi ZHU, mqzhu@tongji.edu.cn
Long ZHOU, https://orcid.org/0000-0003-3379-9771

Received July 9, 2024; Revision accepted Dec. 29, 2024; Crosschecked July 21, 2025; Online first Sept. 11, 2025

lateral unloading than to overload conditions. Zhou et al. (2022) conducted a full-scale experiment for a shield tunnel bearing inner water pressure, and proposed that the damage characteristics of the shield lining under the lateral unloading condition are the waterproof failure of the segmental and ring joints, as well as concrete cracking failure. Also, Chen et al. (2020), Wu et al. (2022, 2023), and Gao et al. (2024) analyzed the structural responses and failure processes of shield lining structures under upper overload and unloading conditions using refined 3D finite element (FE) models. In their research, the lining deformation and stiffness, internal forces (bending moment and axial force) of the lining rings, joint deformation and waterproof performance, and development of concrete cracks were studied. As such, four stages of change in the lining rings were revealed (the linear growth stage, quasi-linear growth stage, nonlinear growth stage, and failure stage). In addition, Su et al. (2022) investigated the internal force distribution and transverse deformation characteristics of a shield tunnel lining subjected to local soil loosening using numerical modeling.

Experimental and numerical studies have provided valuable insights into the structural responses and failure mechanisms of shield lining rings under various loading conditions, revealing the progressive stages of behavior and the importance of joint integrity. However, existing research has often focused on the mechanical behavior and failure mechanisms of isolated or multiple lining rings under changing load scenarios, which may not fully represent the behavior of an entire tunnel under localized load changes. Applying such a method is equivalent to a subsequent load when changes in the surrounding environment are applied to the full-line of a shield tunnel, which is different from actual engineering situations. In practice, shield tunnels can span several kilometers, and it is unlikely that a uniform overload would occur across their entire length. The behavior of a portion of the lining under localized overload differs significantly from a full-line overload scenario (Arnau and Molins, 2015). Additionally, previous studies have been limited by using shell elements and shell interface elements to represent segments and joints, which do not account for detailed 3D structural characteristics, making it impossible to accurately describe the spatial structural characteristics of the shield segmental linings (Arnau and Molins, 2015).

This study aims to overcome existing limitations by developing refined 3D FE models. These models will enable analysis of the mechanical behavior and failure mechanisms of shield segmental linings subjected to localized overload conditions. Additionally, we incorporate practical reinforcement methods that are crucial for bolstering the structural integrity of shield tunnels. The standard approach for mitigating large deformation in shield tunnel linings involves affixing steel rings to the inner surfaces of the lining segments (Liu et al., 2022; Li et al., 2023, 2024; Zhai et al., 2023). We employ two distinct reinforcement strategies: embedding steel rings within each lining ring, and configuring steel rings to span multiple adjacent lining rings (Liu et al., 2020, 2025). By comprehensively evaluating the impact of reinforcement, an optimal reinforcement strategy for scenarios characterized by localized overload is formulated.

2 Finite element model and validation

2.1 Establishment of the finite element model

The numerical simulation focuses on shield lining structures within the Jinan Metro R2 Line, as illustrated in Fig. 1. The segmental lining of the Jinan Metro R2 Line is defined by its precise geometric specifications: an outer diameter of 6.4 m, an inner diameter of 5.8 m, a uniform thickness of 0.3 m, and a width of 1.2 m. Each ring of the lining structure is comprised of a single key segment (referred to as ‘K’), accompanied by two adjacent segments (denoted as ‘L1’ and ‘L2’), and complemented with three standard segments (labeled ‘A1’, ‘A2’, and ‘A3’). The key segment is characterized by a central angle of 22.50°, in contrast to the adjacent and standard segments, which each possess a central angle of 67.50°. The assembly of the lining rings is executed in a staggered-jointed fashion, with a staggered angle of 45.00°, as depicted in Fig. 1.

The ABAQUS software was used for the numerical simulation in this study. The concrete utilized in the lining structures is grade C50, with an elastic modulus of 34.5 GPa and a Poisson’s ratio of 0.2. The concrete behavior is modeled using a plastic damage model, with specified tensile and compressive strengths of 2.64 MPa and 32.40 MPa, respectively. Fig. 2 delineates the stress–strain relationship, as well as the strain and damage parameters of the concrete material. The

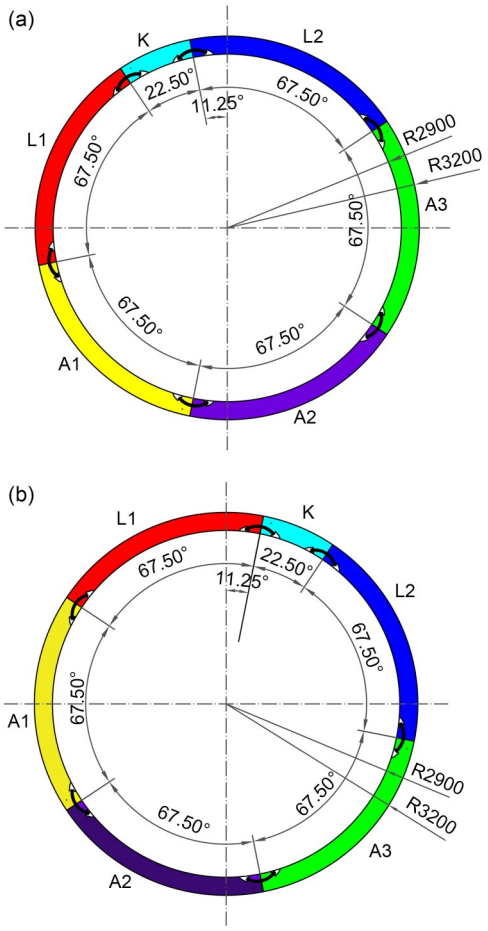

Fig. 1 Shield segmental lining diagram (unit: mm): (a) lining ring with key segment on left side; (b) lining ring with key segment on right side. References to color refer to the online version of this figure

simulation of concrete segments employs eight-node linear solid elements (type C3D8R). In the case of steel bars in the segments, the simulation considers only the main steel bars along the circular lining rings, with the transverse stirrups being excluded from the analysis. The strength grade of the main steel bars is HPB400 with a yield strength of 400 MPa, an elastic modulus of 210 GPa, and a Poisson's ratio of 0.3. Fig. 3a shows the relationship between stress and strain for the HPB400 steel bars.

The main longitudinal steel bars are embedded within the concrete model, with their simulation facilitated through two-node truss elements (type T3D2). Two circumferential curved bolts with Grade 6.8 and a diameter of 27 mm are applied to connect the segmental joint between the two adjacent segments. Sixteen longitudinal curved bolts with Grade 6.8 and a diameter of 27 mm are used to connect the two adjoining lining rings, with each bolt positioned at an equal angular interval of 22.50°. The yield and ultimate strengths of the Grade 6.8 circumferential and longitudinal bolts are 480 MPa and 600 MPa, respectively. The elastic modulus and Poisson's ratio of the bolts are 210 GPa and 0.3, respectively. Fig. 3b shows the relationship between stress and strain of the bolts. For the simulation of the embedded bolts within the concrete model, a solid element of type C3D8R is utilized. In constructing the 3D FE models for the tunnel lining structures, the water-stop grooves at the segmental and ring joints are intentionally excluded. The ethylene propylene

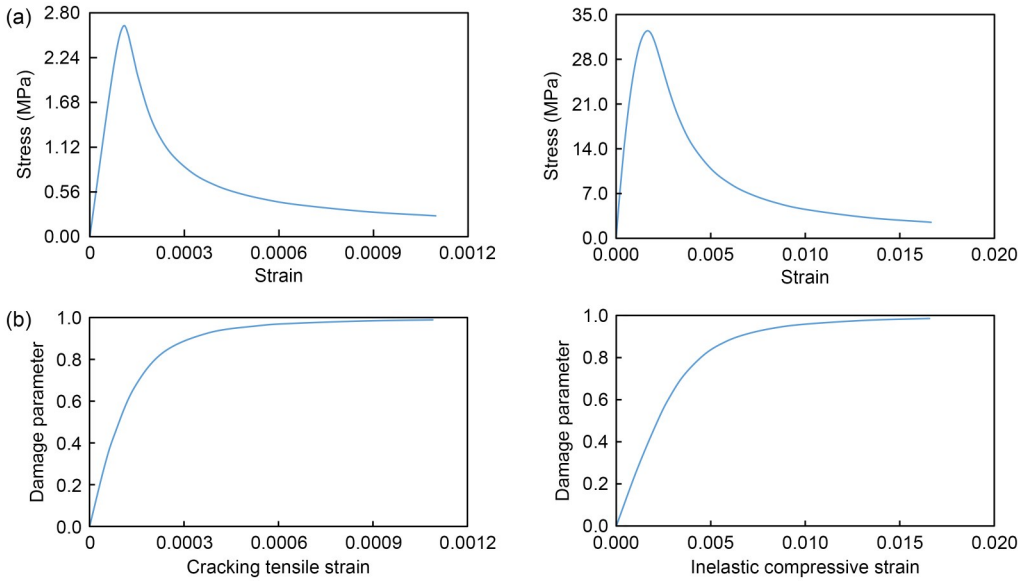

Fig. 2 Concrete plastic damage model (left: tension; right: compression): (a) stress–strain relationship; (b) damage parameter

diene monomer (EPDM) rubber water-stop belts are also omitted from the models. The contact between the segments in the segmental and ring joint positions is realized via the surface-to-surface function in the ABAQUS software, with the parameters set to represent a hard contact in the normal direction and a friction coefficient of 0.5 in the tangential direction. Given the study requirements and computational constraints, seven lining rings were modeled for our analysis. The FE model of the seven assembled rings, including the concrete segments, bolts, and main steel bars, is depicted in Fig. 4.

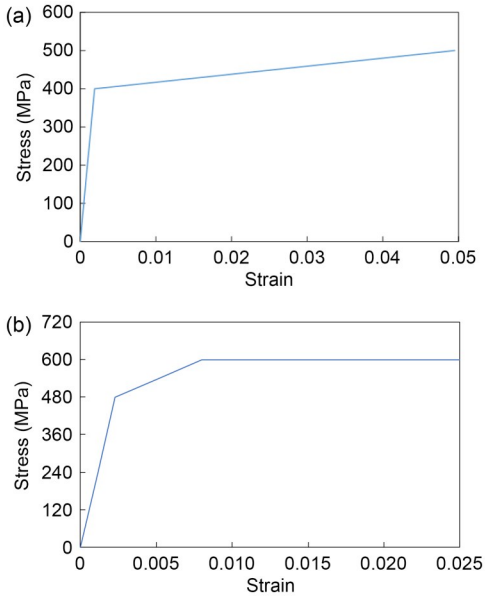

Fig. 3 Stress–strain relationship of steel bars and bolts: (a) steel bar; (b) bolt

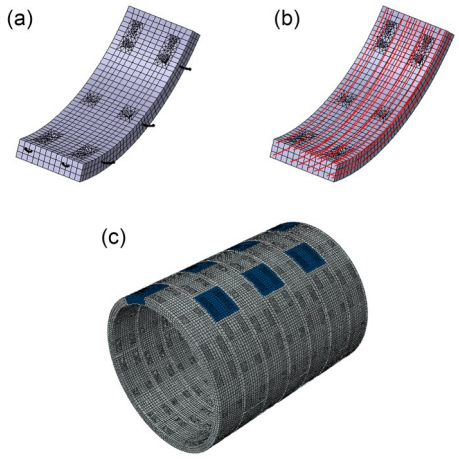

Fig. 4 Numerical model: (a) a segment and bolts; (b) steel bars; (c) seven lining rings. References to color refer to the online version of this figure

2.2 Loading conditions

The Jinan Metro R2 Line is taken as a case study. The largest burial depth of the shield tunnel is 22.5 m, with a surrounding soil weight of 18 kN/m^3 and a lateral earth pressure coefficient of 0.5. In the simulations, the burial depth is fixed at 22.5 m, and the earth pressure on the lining is depicted in Fig. 5. The ground reaction force is simulated by ground springs, and the radial and tangential ground springs are adopted at the outer surface of the lining rings. The radial ground springs have a stiffness k_n of 15000 kN/m^3 in the compressive state and 0 kN/m^3 in the tensile state. According to the 'Standard for Design of Shield Tunnel Engineering (GB/T 51438-2021)', the stiffness k_s of the tangential ground springs is taken as 1/3 of the radial ground spring stiffness (MOHURD, 2021). In Fig. 5, g represents the self-weight of the lining. Previous studies indicate that the longitudinal stress between rings can exceed 1.2 MPa (Liu et al., 2021). Thus, in the simulations, we set the minimum longitudinal stress between adjacent rings at 1.2 MPa.

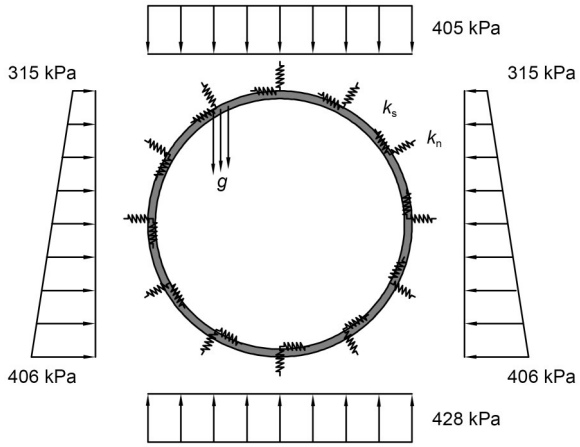

Fig. 5 Loading on lining structures

To assess the effects of localized versus full-line overload on the structural behavior of lining rings, two distinct loading scenarios are modeled with the FE method as shown in Fig. 6. The first scenario involves a top overload ΔP on three consecutive rings (Rings 3−5), simulating a localized overload. The second scenario applies ΔP to all seven rings (Rings 1−7), representing a full-line overload. The simulation sequence begins with the application of existing earth pressure (Fig. 5) and longitudinal stress of 1.2 MPa to establish the post-construction stress and deformation state of the

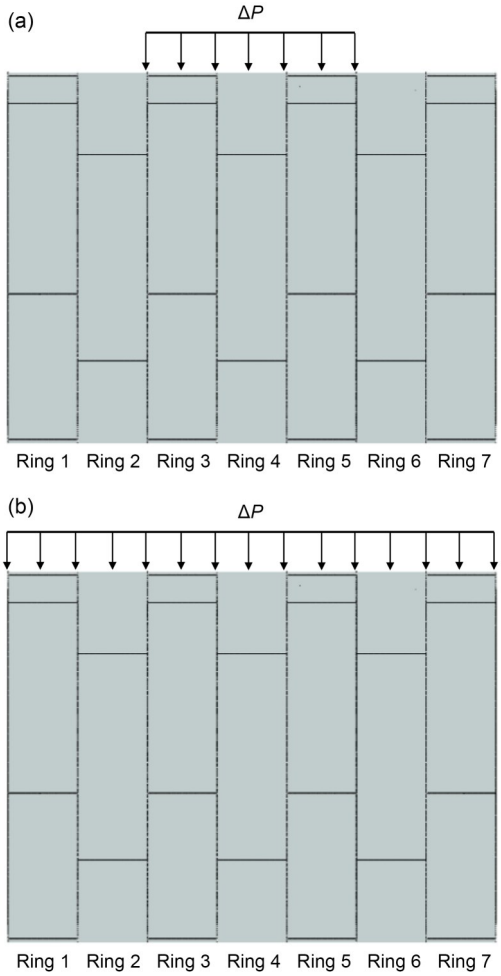

Fig. 6 Overload conditions: (a) localized overload on three lining rings; (b) full-line overload on seven lining rings

lining rings. Subsequently, the top overload ΔP is incrementally applied to the specified rings at levels of 100 kPa, 200 kPa, and 300 kPa.

2.3 Validation with a segmental joint bending experiment

To validate the numerical models, a bending experiment on a segmental joint of a lining ring was performed. The length of the segment in the experiment is 1/3 of the standard segment, and the two segments are assembled to form a segmental joint. The center angle of the experimental segment is 22.50°, with a thickness of 0.3 m and a width of 1.2 m. The strength grade of the segment concrete, the longitudinal main reinforcement arrangement, the hand hole size, and the bolt strength and size are all the same as those described in Section 2.1. The experiment is conducted using a loading system designed for shield tunnel joints at Tongji University, China. The setup includes a self-balancing frame, vertical and horizontal actuators, supports, and a controller, and is capable of bi-directional loading. The joint's internal forces, excluding the specimen's self-weight, are calculated as follows: bending moment M=0.7P−0.0936F, where P and F are the vertical and horizontal loads applied by the respective actuators, and the value of axial force N equals the value of horizontal loads F. The details of the segmental joint bending experiment are shown in Fig. 7.

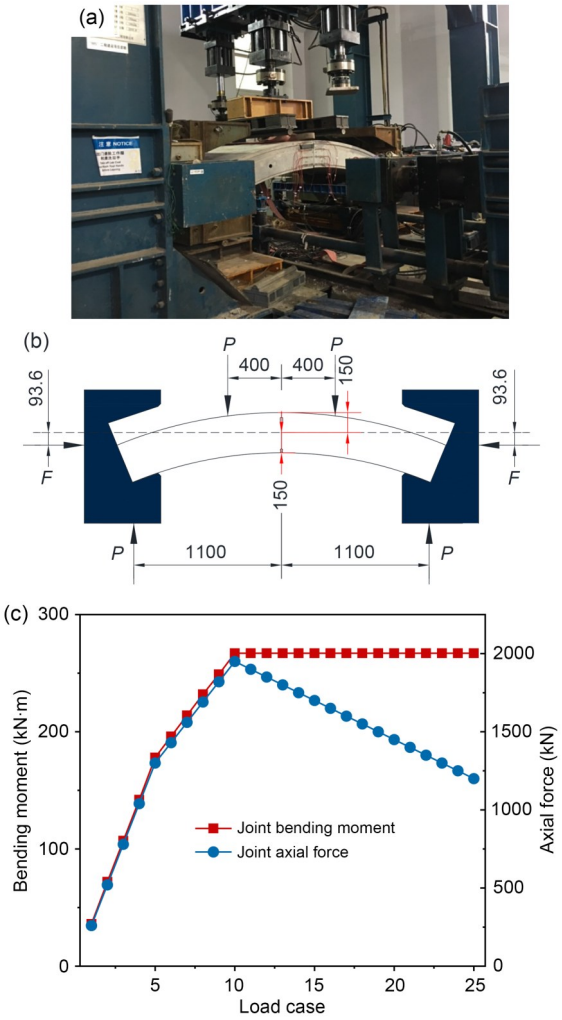

Fig. 7 Details of the segmental joint bending experiment: (a) loading equipment; (b) loading mode (unit: mm); (c) bending moment and axial force at joint position. References to color refer to the online version of this figure

When constructing the segmental joint model in ABAQUS software, the material properties and dimensions are consistent with those of the bending experimental setup. As with the lining ring model detailed in

Section 2.1, the joint model omits water-stop grooves and EPDM rubber water-stop belts. A depiction of the model is presented in Fig. 8. In the loading process, the values and positions of the applied loads are the same as those in the bending experiment.

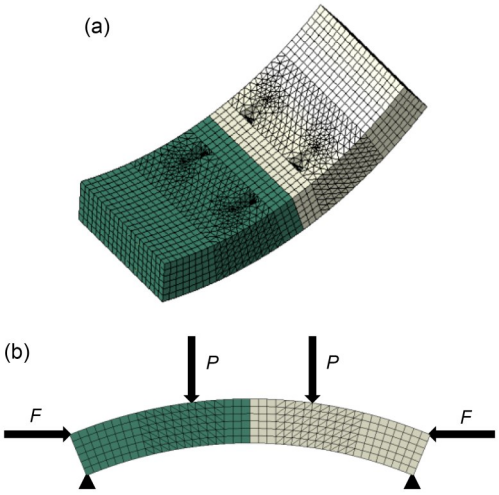

Fig. 8 Segmental joint numerical model: (a) segmental joint; (b) loading. References to color refer to the online version of this figure

Numerical calculation results of the segmental joint opening are compared to experimental data. As depicted in Fig. 9, the numerical result closely mirrors the experimental pattern of the joint opening. At a constant bending moment of 267 kN·m, a reduction to 1700 kN in axial force initiates joint opening in both the numerical model and the bending experiment. The numerical model predicts joint failure at an axial force of 1500 kN, which is a 3.2% discrepancy from the experimental failure force of 1550 kN. This variance may stem from the exclusion of features like water-stop grooves and EPDM rubber belts in the numerical model. Fig. 10 illustrates the compressive

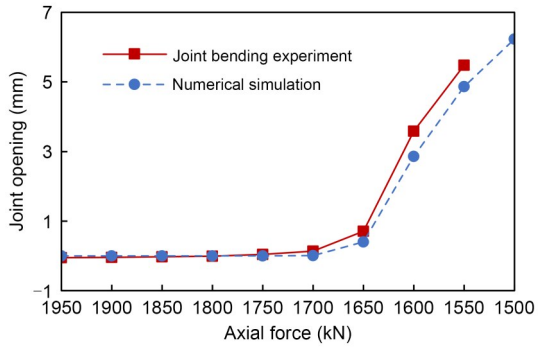

Fig. 9 Comparison of joint opening

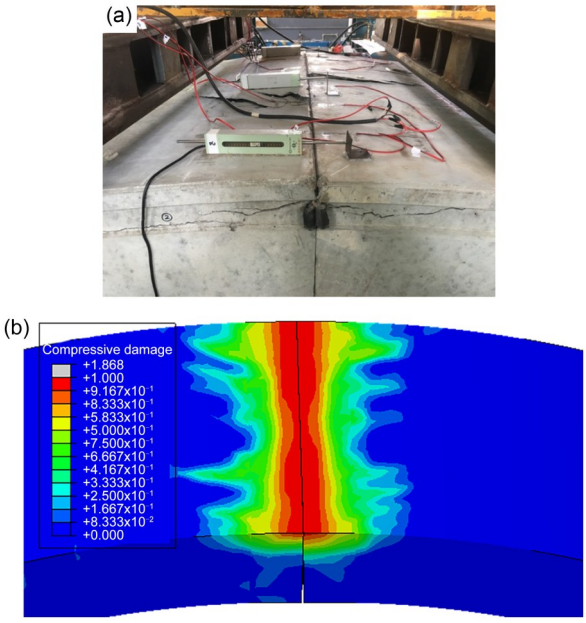

Fig. 10 Comparison of concrete failure: (a) experimental result; (b) numerical simulation result. References to color refer to the online version of this figure

damage area during joint failure, with the numerical model closely aligning with experimental observations. Given the congruence in the joint opening patterns (Fig. 9) and the compressive damage areas (Fig. 10), the numerical model is deemed accurate for simulating the experiment results and representing the stress conditions of the joint.

3 Performance of shield segmental linings under localized overload

3.1 Deformation and internal force of the lining rings

The numerical models encompass seven shield-lining rings. Given the symmetry of the Rings 1−3 and Rings 5−7 lining rings with respect to central Ring 4, our deformation and internal forces analyses focus on the four rings from Ring 1 to Ring 4. When subjected to a top overload, the lining rings exhibit a horizontal egg-shaped deformation pattern, which means the distance between the tunnel crown and the tunnel bottom (vertical convergence deformation) decreases, while the distance between the two sides of the tunnel waists (horizontal convergence deformation) increases. In the overloading process, the horizontal convergence deformation exceeds the vertical convergence deformation in

magnitude. Fig. 11 delineates the pattern of horizontal convergence deformation for Rings 1−4 as the overload is applied. Additionally, Fig. 12 illustrates the deformation profile of these rings under a 300 kPa overload scenario.

The deformation of the lining rings under full-line overload is notably higher than that under localized overload, as shown in Figs. 11 and 12. For the same overload level, the convergence deformation of the lining under full-line overload is 1.5 to 2.0 times higher than that under localized overload. Under full-line overload, all lining rings converge uniformly, but with localized overload, the deformation varies. Specifically, when Rings 3−5 are overloaded, they show more similar and larger deformations compared to Rings 1, 2, 6, and 7. The deformation diminishes with increasing distance from the overloaded Rings 3−5. At a localized overload of 300 kPa, the deformations for Rings 4, 3, 2, and 1 are 50.20 mm, 50.20 mm, 46.07 mm, and 43.19 mm, respectively.

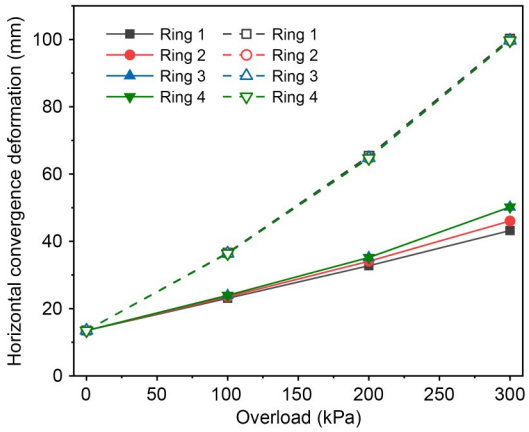

Fig. 11 Lining deformation. The solid line and the dotted line respectively represent the localized overload and the full-line overload scenarios

Fig. 13 illustrates the internal force (bending moment and axial force) changes in Rings 1−4 during the overloading process, with 0° and 180° indicating the tunnel crown and bottom, and 90° and 270° indicating the tunnel waist sides. The bending moment and axial force in each lining ring increase with larger overload, in both the full-line and localized overload scenarios. For a 300 kPa overload, the internal force and corresponding lining deformation for Rings 1−4 are shown in Table 1. When overloaded, linings deform towards the soil, which reacts with increasing force as deformation grows. Full-line overloads cause greater deformation, and thus higher bending moments and axial forces, compared to localized overloads (Table 1). For full-line overloads, Rings 1−4 show similar deformations (100.20 mm, 99.69 mm, 99.69 mm, and 99.69 mm) and naturally have similar forces. However, under localized overload, Rings 4 and 3 experience higher forces

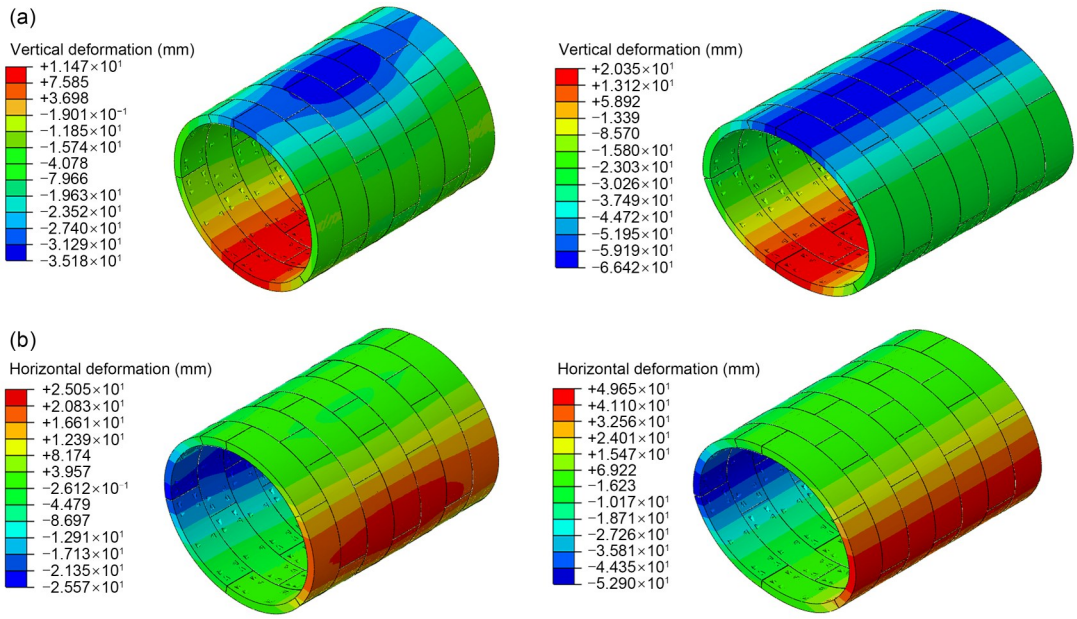

Fig. 12 Lining deformation (unit: mm; deformation magnification: 10 times): (a) vertical convergence deformation; (b) horizontal convergence deformation. Left: 300 kPa overload on Rings 3−5; right: 300 kPa overload on Rings 1−7. References to color refer to the online version of this figure

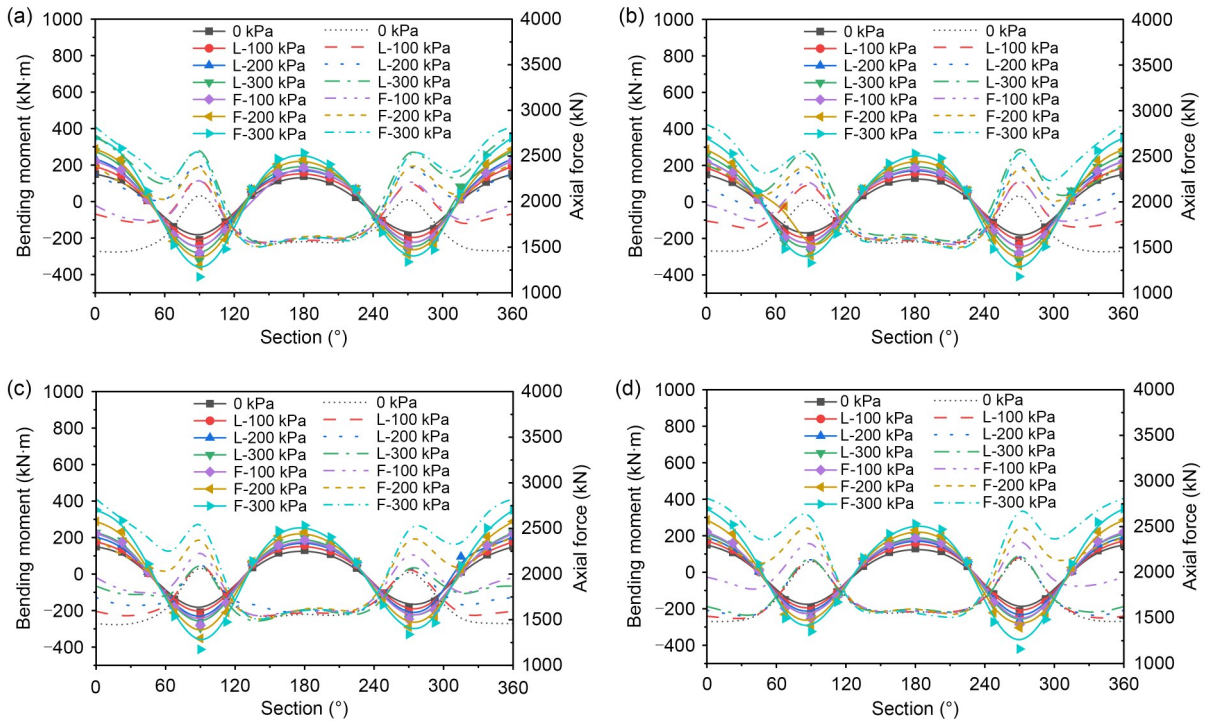

Fig. 13 Lining internal force: (a) Ring 4; (b) Ring 3; (c) Ring 2; (d) Ring 1. L and F mean overload on Rings 3–5 and Rings 1–7, respectively. Solid and dotted lines represent bending moment and axial force, respectively

Table 1 Internal force and corresponding lining deformation for Rings 1–4 at 300 kPa overload

Ring	Full-line overload			Localized overload		
	Bending moment (kN·m)	Axial force (kN)	Deformation (mm)	Bending moment (kN·m)	Axial force (kN)	Deformation (mm)
Ring 4	−413–350	1435–2838	99.69	−324–276	1512–2843	50.20
Ring 3	−409–350	1443–2848	99.69	−320–255	1564–2880	50.20
Ring 2	−413–351	1439–2834	99.69	−295–227	1447–2300	46.07
Ring 1	−413–351	1485–2939	100.20	−291–209	1488–2397	43.19

due to greater deformations (50.20 mm and 50.20 mm for Rings 4 and 3 versus 46.07 mm and 43.19 mm for Rings 2 and 1).

In summary, the analysis reveals that localized overload simulation produces a more varied response, with stronger forces concentrated in the immediate vicinity of the overload. The difference in these forces for full-line and localized overload scenarios highlights the importance of understanding the conditions and distribution of the overload when assessing the structural integrity and safety of tunnel linings. Thus, our analysis suggests that when simulating the mechanical behaviors and failure mechanisms of lining rings under loading conditions, it is crucial to use the FE model with localized overload.

3.2 Joint deformation and bolt stress

Next, we discuss segmental joint opening and ring joint dislocation of the lining rings when subjected to localized overload. The joint deformation and bolt stress escalate with an increase in lining ring deformation. Fig. 14 shows the maximum values of joint deformation and stress of bolts at different ring positions. Fig. 15 illustrates the segmental joint opening in Ring 4 under a 300 kPa overload. Larger joint openings occur at the tunnel bottom, which experiences positive bending moments, as well as at the tunnel waist, which experiences negative bending moments. Circumferential bolts, which are positioned near the segmental joints' inner sides, restrict joint openings. Their constraining effect is stronger on the inner sides

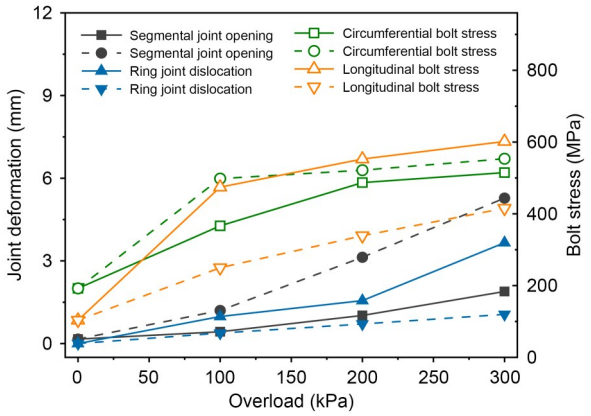

Fig. 14 Maximum joint deformation and bolt stress. The solid line and the dotted line respectively represent the localized overload and the full-line overload scenarios

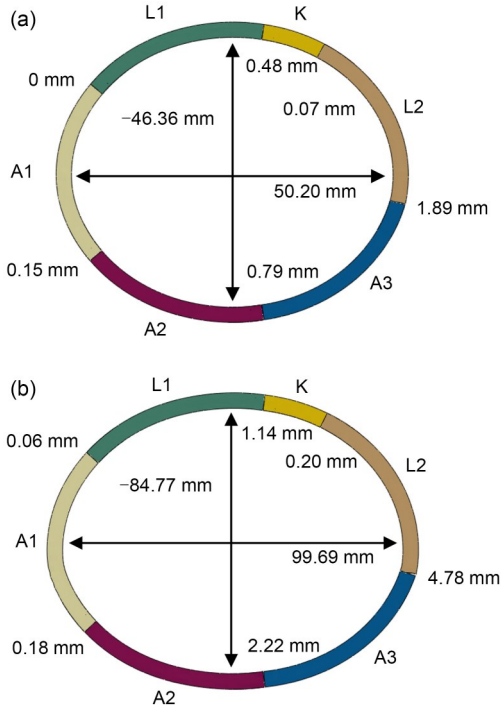

Fig. 15 Segmental joint opening in Ring 4 (deformation magnification: 10 times): (a) 300 kPa overload on Rings 3–5; (b) 300 kPa overload on Rings 1–7

of the joints compared to the outer sides, leading to the largest joint opening occurring at the tunnel waist under negative bending. As depicted in Fig. 15, the L2–A3 joint opening measures 1.89 mm under localized overload at 300 kPa, contrasting with a 4.78 mm joint opening under full-line overload. The stress on circumferential bolts at the joints of locally overloaded lining rings is lower than that in full-line overload scenarios, which is due to the smaller joint openings.

Fig. 14 indicates that the maximum circumferential bolt stress in the lining rings reaches 553.6 MPa under full-line overload, surpassing the 514.8 MPa observed under localized overload conditions; however, localized overload poses a greater risk to the structural integrity of lining rings due to increased joint dislocation and bolt stress. Under full-line overload, deformation is uniform across all lining rings, leading to minimal joint dislocation (maximum 1.06 mm), while with localized overload, Ring 3 and Ring 4 show greater deformation (50.20 mm for both) than Ring 2 and Ring 1 (46.07 mm and 43.19 mm), causing significant joint dislocation (maximum 3.66 mm) between adjacent rings. The stress on longitudinal bolts at ring joints in localized overload (maximum 601.6 MPa) is higher than that in full-line overload (415.3 MPa), due to greater joint dislocation.

3.3 Concrete plastic strain and steel bar stress

The plastic strain in the concrete of the shield lining rings is depicted in Fig. 16, for an overload of 300 kPa. Notably, the concrete experiences tensile strain at the inner surfaces of the tunnel crown and bottom,

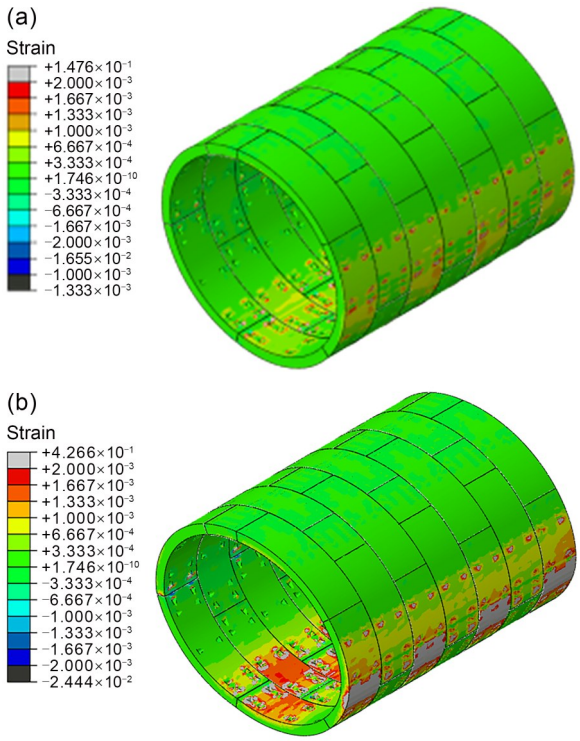

Fig. 16 Concrete plastic strain distribution (deformation magnification: 10 times): (a) 300 kPa overload on Rings 3–5; (b) 300 kPa overload on Rings 1–7. References to color refer to the online version of this figure

and at the outer surfaces of the tunnel waists, where plastic strain is substantial. This is due to the positive and negative bending moments putting the concrete in a tensile state. Furthermore, significant plastic compressive strain is observed at the segmental joints near the tunnel waists, while substantial plastic tensile strain occurs around certain bolt handholes. The former phenomenon is attributed to the opening of the external sides of the joints, compressing the internal concrete. The latter is due to the tensile load from the bolts when the joints open or dislocate, affecting the concrete at handhole locations.

Fig. 17 presents the stress distribution in the steel bars of Ring 4, which exhibits the greatest deformation among the seven rings. The steel bars in Ring 4 experience higher stress at the tunnel crown and bottom, and at both sides of the tunnel waists. The positive bending moments at the crown and bottom result in tensile stress in the steel bars near the inner surface, and compressive stress in the bars near the outer surface. Conversely, at the tunnel waists with negative bending moments, the outer surface steel bars are under tension, and the inner surface bars are under compression.

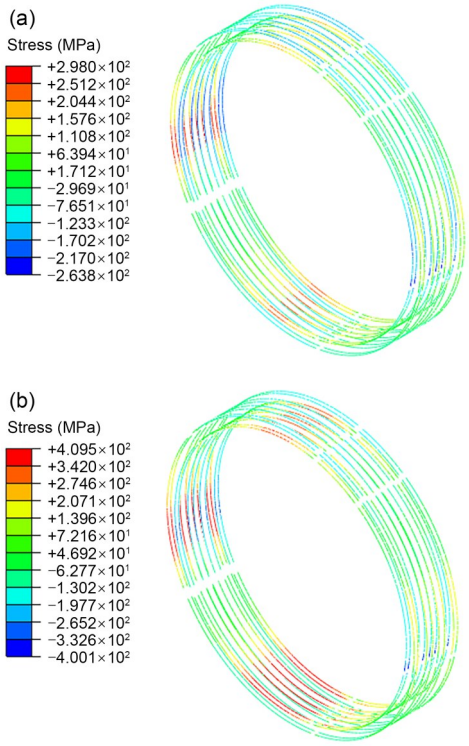

Fig. 17 Stress distribution of the steel bars in Ring 4: (a) 300 kPa overload on Rings 3–5; (b) 300 kPa overload on Rings 1–7. References to color refer to the online version of this figure

Due to the fact that the deformation of Ring 4 in the full-line overload scenario of 300 kPa is greater than that in the localized scenario with the same overload value, the plastic strain distribution area of the concrete (Fig. 16) and maximum stress of the steel bars (Fig. 17) under localized overload are smaller than those under full-line overload. These maximum stresses of the tensile and compressive reinforcements are 298.0 MPa and 263.8 MPa, compared to 409.5 MPa and 400.1 MPa, respectively.

3.4 Discussion of the failure characteristics of lining rings

The analysis from Sections 3.1 to 3.3 indicates that when a shield tunnel is subjected to a full-line overload of 300 kPa, the deformation of the lining rings, the opening of the segmental joints, the stress on circumferential bolts at the segmental joints, the extent of the plastic zone in the segmental concrete, and the stress on the main longitudinal steel bars are all greater than those under a localized overload of the same magnitude. Conversely, ring joint dislocation and the stress on longitudinal bolts at ring joints are lower under full-line overload, showing the opposite relationship compared to localized overload conditions.

For the shield segmental linings, which are composed of prefabricated reinforced concrete segments and bolts, the segmental and ring joints are identified as the weak points. Failure of these joints, particularly when bolts break, can lead to a continuous collapse within the lining structure, as cited by Liu et al. (2016, 2017) and Gao et al. (2024). The bolts in the shield lining structures of the Jinan Metro R2 Line have a yield strength of 480.0 MPa and an ultimate strength of 600.0 MPa. Under full-line overload, the maximum stress at the circumferential bolts reaches 553.6 MPa, surpassing the yield strength and entering the plastic deformation phase, while the stress at the longitudinal bolts remains at 415.3 MPa within the elastic stage. Under localized overload, the circumferential bolts experience a maximum stress of 514.6 MPa and also enter the plastic deformation phase, whereas the longitudinal bolts are subjected to 601.6 MPa of stress, indicating potential damage.

It is evident that when only certain lining rings in the tunnel are overloaded, significant dislocation can occur at the ring joints between the overloaded and adjacent non-overloaded rings; this may lead to bolt

stresses exceeding their ultimate strength and result in bolt failure. This suggests that the primary risk of failure for shield segmental lining rings originates from bolt failure at the ring joint positions. Therefore, when examining the mechanical properties of shield segmental linings under localized overload (which is a more common scenario in practice), it is crucial to thoroughly consider the impact of ring joint dislocation and the stress in longitudinal bolts at ring joints on the structural integrity and failure characteristics of the linings.

4 Reinforcement of shield segmental linings under localized overload

4.1 Reinforcement measures

The standard approach for mitigating large deformation issues in shield tunnel linings involves affixing steel rings to the inner surfaces of the lining rings. This technique creates a composite system that enhances the overall rigidity and load-bearing capacity of the tunnel (Liu DJ et al., 2020, 2025; Liu TJ et al., 2022; Li et al., 2023, 2024; Zhai et al., 2023). Fig. 18 presents two different reinforcement strategies which we will model numerically: one involving steel rings placed within individual lining rings, and another with steel rings spanning two adjacent rings. The steel rings have an outer diameter of 5.8 m and a uniform thickness of 20 mm. For the internal reinforcement scheme (referred to as the 'inside ring reinforcement scheme'), each lining ring is equipped with a steel ring that is 1.1 m wide, resulting in a total of seven such rings within the structure, as depicted in Fig. 18a. The spanning reinforcement scheme (referred to as the 'spanning ring reinforcement scheme') features steel rings that are also 1.1 m wide, but instead span across two adjacent lining rings, totaling six steel rings. Additionally, a narrower steel ring, measuring 0.55 m in width, is placed within the first and seventh rings, as depicted in Fig. 18b. It is important to note that in both reinforcement schemes, the cumulative weight of the steel rings is the same.

For the numerical models, the dimensions, materials, and methods for establishing the components of the seven lining rings are the same as described in Section 2.1. The material of the steel rings is Q345 steel with a yield strength of 345 MPa, an elastic

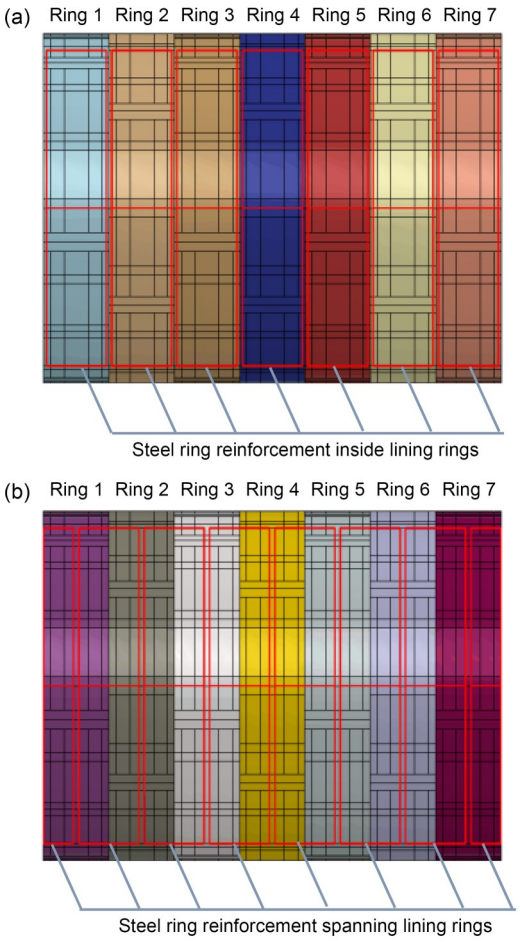

Fig. 18 Reinforcement measures for lining rings: (a) inside ring scheme; (b) spanning ring scheme. References to color refer to the online version of this figure

modulus of 210 GPa, and a Poisson's ratio of 0.3. The simulation of the steel rings employs solid elements of type C3D8R. The interaction between the outer surface of the steel rings and the inner surface of the lining rings is achieved by setting a 'Cohesive Behavior' in the ABAQUS software. The interfacial parameters between the lining rings and steel rings are drawn from existing literature (Liu et al., 2025), with a normal stiffness set to 144 MPa/mm and a tangential stiffness set to 40 MPa/mm; other specific parameters can be found in (Li et al., 2024). The numerical models of shield segmental linings strengthened by steel rings for the two reinforcement schemes are shown in Fig. 19. The applied localized overload in the numerical models is the same as used in Section 2.2. The construction of steel rings is set to occur after the application of the overload shown in Fig. 5, and the longitudinal stress of 1.2 MPa is applied to the lining rings. The workflow

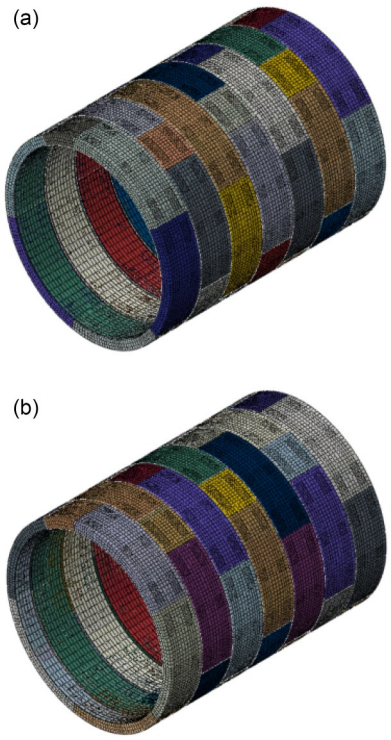

Fig. 19 Numerical models of segmental lining rings strengthened by steel rings: (a) steel rings inside lining rings; (b) steel rings spanning lining rings. References to color refer to the online version of this figure

is as follows: (1) first, the 'Model Change' function in the ABAQUS software is used to set the steel ring to the inactive state; (2) then, the load shown in Fig. 5 and the longitudinal stress of 1.2 MPa are applied to the segmental lining rings; (3) finally, the steel rings are activated and the top overload ΔP (shown earlier in Fig. 6a) is subsequently applied.

The linings of Rings 1–4 are investigated in terms of deformation and internal forces due to their symmetry with the reinforced rings from Rings 5–7, on either side of the central Ring 4. These rings show a 'horizontal egg'-shaped deformation pattern, where the horizontal deformation exceeds the vertical deformation under localized overload. Fig. 20 illustrates the horizontal deformation trend for Rings 1–4, while Fig. 21 shows their deformation under a 300 kPa localized overload. These results indicate that both reinforcement schemes significantly reduce horizontal convergence deformation under a 300 kPa localized overload. Specifically, for the inside ring reinforcement scheme, the deformations for Rings 1–4 are 23.96 mm, 25.71 mm, 28.76 mm, and 29.05 mm, respectively. In contrast, for the spanning ring reinforcement scheme,

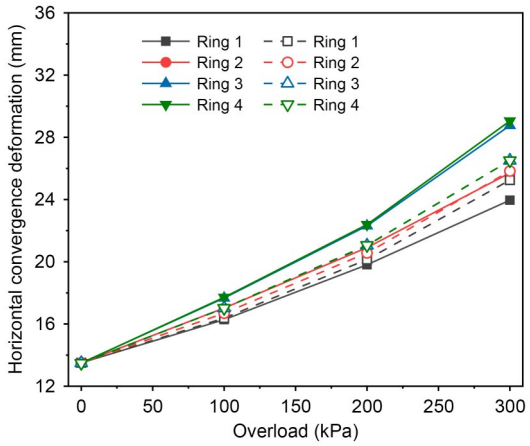

Fig. 20 Horizontal convergence deformation of reinforced lining rings. Solid and dotted lines represent the inside and spanning ring reinforcement schemes, respectively

these deformations are slightly lower at 25.25 mm, 25.83 mm, 26.51 mm, and 26.51 mm. This reduction in deformation ranges from 40% to 50% compared to the un-reinforced scenario, where the deformations are 43.19 mm, 46.07 mm, 50.20 mm, and 50.20 mm for Rings 1–4, respectively.

The inside ring reinforcement scheme enhances the stiffness of individual rings but does not effectively restrict joint dislocation between adjacent rings. Conversely, the spanning ring reinforcement scheme increases ring stiffness and leverages longitudinal bolts at joint positions to control joint dislocation. This results in a more uniform deformation across adjacent rings. For instance, under a 300 kPa overload, the difference in deformation between overloaded Ring 3 and adjacent Ring 2 without overload is 3.05 mm for the inside ring scheme, but only 0.32 mm for the spanning ring scheme. This highlights the superior performance of the spanning ring reinforcement in minimizing deformation disparities between neighboring rings.

Fig. 22 compares the bending moments and axial forces in the lining rings of Rings 1–4, both with and without steel ring reinforcement, under a 300 kPa localized overload. The data reveal that reinforcement with steel rings leads to a reduction in both the bending moment and axial force for each ring; however, the bending moments and axial forces are nearly identical for the lining rings at the same position, regardless of which reinforcement scheme is used. The reduction rates of the maximum negative and positive bending moments and the maximum axial force are shown in Table 2. The maximum reduction rates of the

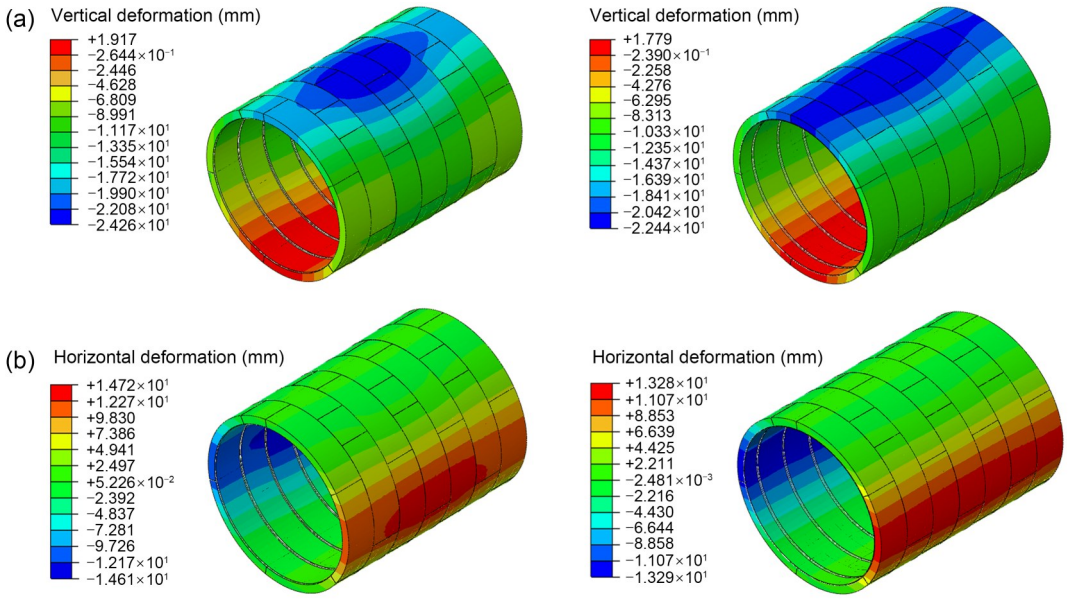

Fig. 21 Deformation of reinforced lining rings with localized overload of 300 kPa (deformation magnification: 10 times): (a) vertical deformation; (b) horizontal deformation. Left: inside ring reinforcement scheme; right: spanning ring reinforcement scheme. References to color refer to the online version of this figure

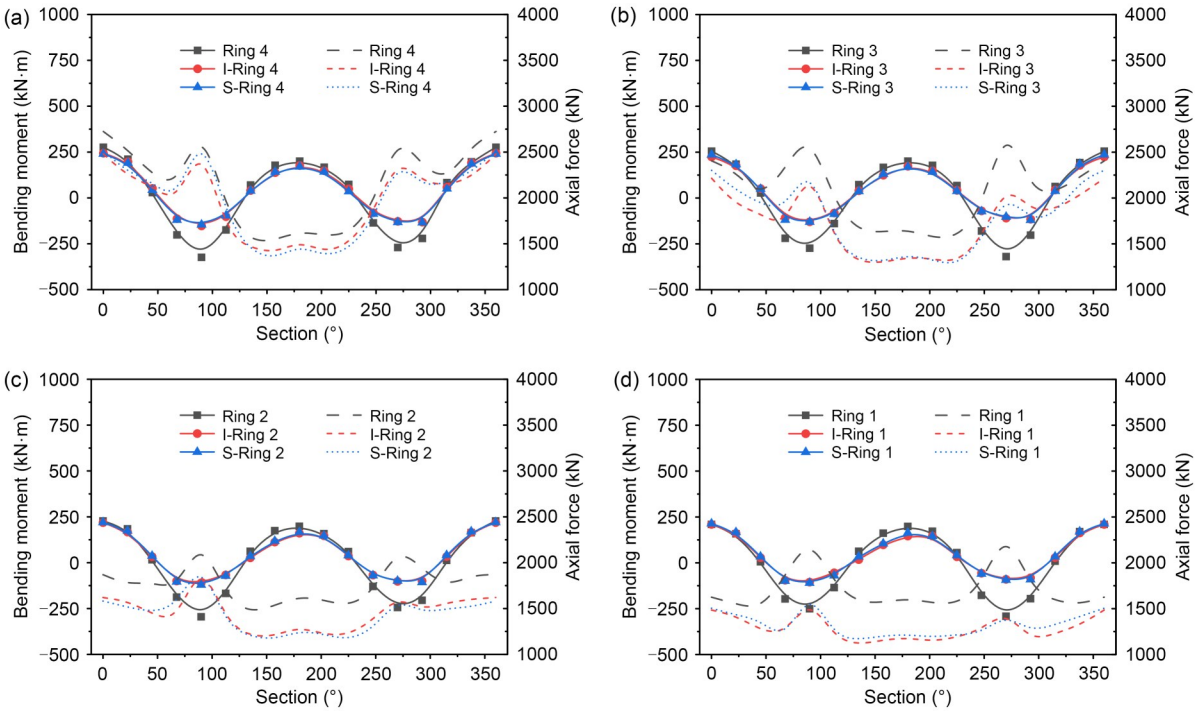

Fig. 22 Comparison of bending moment and axial force in lining rings with and without steel ring reinforcement under a localized overload of 300 kPa: (a) Ring 4; (b) Ring 3; (c) Ring 2; (d) Ring 1. I and S refer to the inside and spanning ring reinforcement schemes, respectively. Solid and dotted lines represent the bending moment and axial force, respectively

negative bending moment, positive bending moment, and axial force for the inside reinforcement scheme are 63.9%, 12.2%, and 31.9%, and those for the spanning reinforcement scheme are 59.1%, 13.0%, and 27.7%, respectively. There are two reasons for this internal force reduction. The first is that the steel ring reinforcement reduces the deformation of the shield lining by decreasing the ground reaction force. In addition,

Table 2 Internal force reduction for reinforced lining rings

Ring	Non-reinforced		Reinforced with steel rings inside lining rings			Reinforced with steel rings span lining rings		
	Bending moment (kN·m)	Axial force (kN)	Bending moment (kN·m)	Axial force (kN)	Reduction rates of maximum negative and positive bending moments and maximum axial force (%)	Bending moment (kN·m)	Axial force (kN)	Reduction rates of maximum negative and positive bending moments and maximum axial force (%)
Ring 4	−324–276	1512–2843	−153–244	1396–2664	52.8, 11.6, 6.3	−146–240	1334–2780	54.9, 13.0, 2.2
Ring 3	−320–255	1564–2880	−130–224	1291–2397	59.4, 12.2, 16.8	−131–236	1251–2402	59.1, 7.4, 16.6
Ring 2	−295–227	1447–2300	−110–218	1192–2061	62.7, 4.0, 10.4	−121–220	1153–2053	59.0, 3.1, 10.7
Ring 1	−291–209	1488–2397	−105–209	1104–1632	63.9, 0, 31.9	−121–220	1146–1732	58.4, −5.2, 27.7

the reinforced steel rings also share part of the load, leading to a reduction in the internal forces within the lining rings.

Fig. 23 illustrates the maximum segmental joint openings and circumferential bolt stresses at the joint positions, as well as ring joint dislocations and longitudinal bolt stresses at the ring joint positions in the reinforced lining rings of Rings 1–4 under localized overload. The maximum segmental joint opening in the lining rings reinforced with steel rings spanning the lining rings is less than that in the rings reinforced with steel rings inside the lining rings, due to reduced deformation from the spanning reinforcement scheme. Fig. 24 showcases the joint opening distribution in Ring 4, which experiences the greatest deformation among the seven reinforced lining rings under a 300 kPa localized overload. The maximum opening for the L2–A3 segmental joint in Ring 4 is 1.72 mm for the inside ring reinforcement scheme and 1.21 mm for the spanning ring reinforcement scheme. Because the maximum openings of the segmental joints in the lining rings with the inside ring reinforcement scheme are larger, the stresses in circumferential bolts at the segmental joint positions are also greater. Fig. 23 shows that under a 300 kPa localized overload, the maximum circumferential bolt stress reaches 497.3 MPa for the inside ring reinforcement scheme, surpassing the 487.7 MPa for the spanning ring reinforcement scheme.

The reduced deformation disparity between adjacent lining rings results in lower ring joint dislocation for the spanning ring reinforcement scheme as compared to the inside ring reinforcement scheme, as shown in Fig. 21a. The data from Fig. 23 indicates that the maximum ring joint dislocations for the inside ring and spanning ring reinforcement schemes are 2.31 mm and 0.67 mm, respectively. Furthermore, the maximum

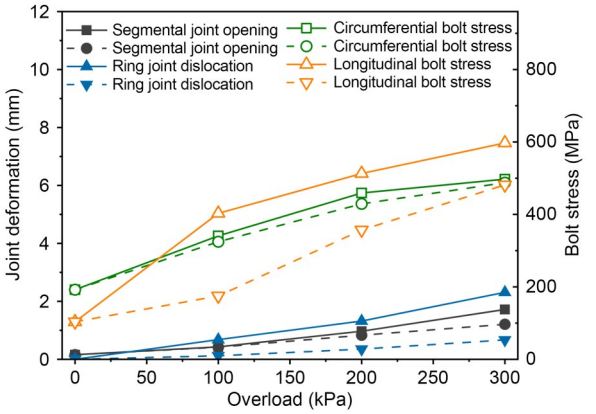

Fig. 23 Maximum joint deformation and bolt stress in reinforced lining rings. Solid and dotted lines represent the inside and spanning ring reinforcement schemes, respectively

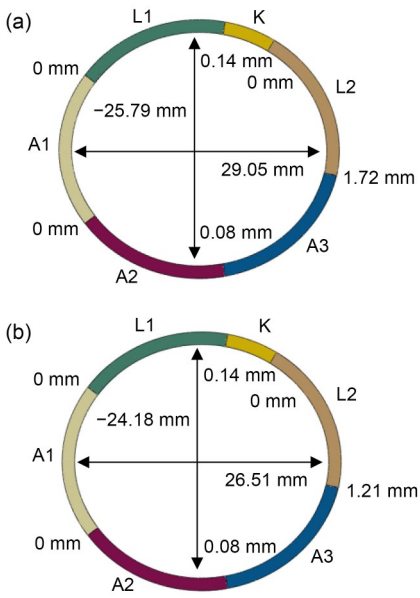

Fig. 24 Segmental joint opening in reinforced Ring 4 (deformation magnification: 10 times): (a) inside ring reinforcement scheme; (b) spanning ring reinforcement scheme

stresses for longitudinal bolts at the ring joint positions in the reinforced lining rings are 597.3 MPa for the inside ring scheme and 481.7 MPa for the spanning ring scheme.

4.2 Discussion of reinforcement effects

Fig. 25 presents the stress distribution in the steel rings for the two reinforcement schemes under a 300 kPa localized overload. It is evident that the stress levels in both schemes are significantly lower than the yield strength of 345 MPa for the rings' Q345 steel. As depicted in Fig. 25a, the steel rings within the lining rings for the inside ring reinforcement scheme experience greater deformation, resulting in a higher maximum von Mises stress of 154.8 MPa. This contrasts with the steel rings of the spanning ring reinforcement scheme, which exhibit a lower maximum von Mises stress of 127.4 MPa. Fig. 25b further illustrates that the maximum hoop stress in the steel rings for the inside ring reinforcement scheme is 108.4 MPa, which exceeds the 73.68 MPa observed in the spanning ring reinforcement scheme. However, the shearing stress in the steel rings is influenced by the differential deformation between adjacent lining rings. As shown in Fig. 25c, the maximum shearing stress for the steel rings in the spanning ring reinforcement scheme is 27.71 MPa, which is notably higher than the 16.42 MPa found within the lining rings for the inside ring reinforcement scheme. This suggests that while the spanning reinforcement scheme may have lower von Mises and hoop stresses, it must also be designed to accommodate the increased shearing stress.

Overall, from evaluating the effects of localized overload on shield tunnel lining structures, the reinforcement scheme in which steel rings span the lining rings proves to be more effective. The spanning reinforcement scheme mitigates joint dislocation and reduces stress on longitudinal bolts, with the reduction in maximum ring joint dislocation ranging from 70% to 82%, and the reduction in maximum longitudinal bolt stress ranging from 19% to 57% compared to the within-ring reinforcement strategy. There are two primary advantages of the spanning steel ring scheme: it enhances the stiffness of each lining ring and effectively restricts dislocation deformation at the ring joints. This restriction is achieved through the steel rings working in conjunction with longitudinal bolts at the ring joint positions, which in turn reduces the stress experienced by the longitudinal bolts. By limiting joint dislocation and sharing the load, the spanning reinforcement scheme minimizes deformation differences between adjacent lining rings, leading to a more uniform and controlled structural response under localized overload conditions.

5 Conclusions

In this study, we utilized 3D FE models to investigate the evolution of mechanical performance and

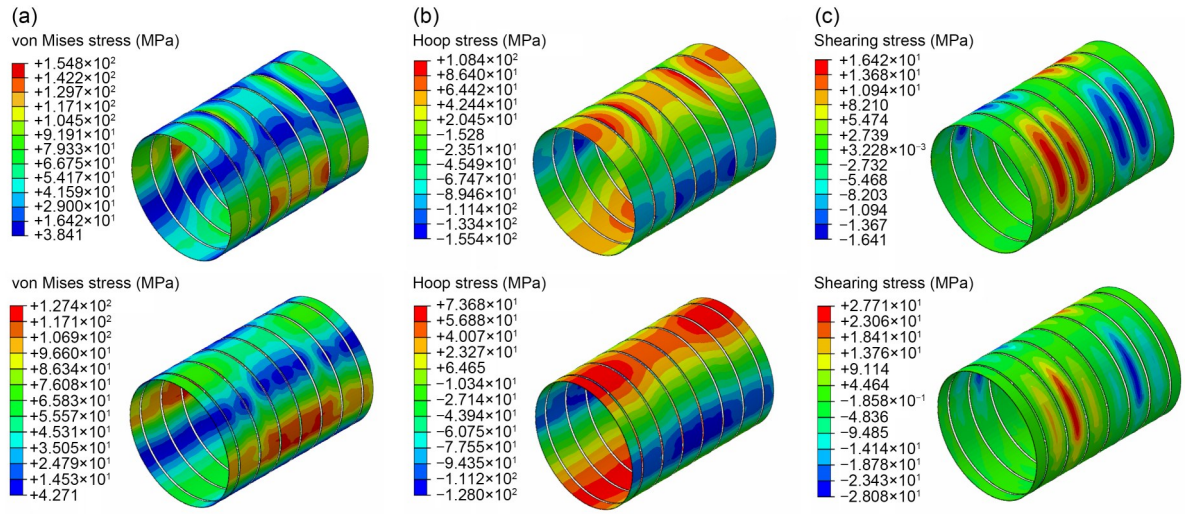

Fig. 25 Stress distribution in the steel rings (deformation magnification: 10 times): (a) von Mises stress; (b) hoop stress; (c) shearing stress. Up: inside ring reinforcement scheme; down: spanning ring reinforcement scheme. References to color refer to the online version of this figure

underlying failure mechanisms in shield segmental lining rings. This investigation compared the effects of localized overload with those of full-line overload. Furthermore, we delved into the reinforcement impact of steel rings placed within individual lining rings and those set to span multiple lining rings, under localized overload conditions. An optimal reinforcement strategy, tailored for localized overload situations, was proposed based on these analyses.

In scenarios where a subset of the shield segmental lining rings is subjected to overload, significant joint dislocation occurs between the overloaded and adjacent non-overloaded rings. This can lead to longitudinal bolt failure when the bolt stress surpasses its ultimate strength. Compared to full-line overload, localized overload results in greater ring joint dislocation and longitudinal bolt stress. However, the deformation of lining rings, the segmental joint opening, the circumferential bolt stress, the extent of plastic zones in segment concrete, and the steel bar stress are comparatively lower. It is therefore imperative to consider the influence of ring joint dislocation and longitudinal bolt stress on the bearing capacity and failure characteristics of the linings in the more common practical scenario of localized overload.

The spanning reinforcement scheme was shown to be more effective among the two tested schemes. This approach results in reduced lining deformation and internal force, segmental and ring joint deformation, circumferential and longitudinal bolt stress, and stress in the reinforcing steel rings as compared to the strategy of installing steel rings within individual lining rings. While employing steel rings within individual lining rings does augment the rigidity of each ring, this strategy falls short in addressing the dislocation of ring joints and the high stress experienced by the longitudinal bolts at these critical points. Conversely, the strategy of using steel rings that span multiple lining rings not only enhances the structural rigidity of each ring, but also mitigates the dislocation at the ring joints and reduces the stress on the longitudinal bolts.

Acknowledgments

This work is supported by the National Natural Science Foundation of China (No. 52008308).

Author contributions

Long ZHOU: conceptualization, methodology, formal analysis, writing–original draft, and funding acquisition. Zhiguo YAN: project administration, supervision, and resources. Mengqi ZHU: investigation, visualization, validation, software, data curation, and writing–review & editing.

Conflict of interest

Long ZHOU, Zhiguo YAN, and Mengqi ZHU declare that they have no conflict of interest.

References

Arnau O, Molins C, 2015. Theoretical and numerical analysis of the three-dimensional response of segmental tunnel linings subjected to localized loads. *Tunnelling and Underground Space Technology*, 49:384-399. https://doi.org/10.1016/j.tust.2015.05.012

Chen RP, Chen S, Wu HN, et al., 2020. Investigation on deformation behavior and failure mechanism of a segmental ring in shield tunnels based on elaborate numerical simulation. *Engineering Failure Analysis*, 117:104960. https://doi.org/10.1016/j.engfailanal.2020.104960

Elbady A, Mousa S, Mohamed HM, et al., 2023. Effect of test parameters on the punching-shear strength of precast tunnel segments reinforced with GFRP bars. *Engineering Structures*, 297:117016. https://doi.org/10.1016/j.engstruct.2023.117016

Gao BY, Chen RP, Wu HN, et al., 2024. Investigation of mechanical failure performance of a large-diameter shield tunnel segmental ring. *Journal of Zhejiang University-SCIENCE A*, 25(5):411-428. https://doi.org/10.1631/jzus.A2300446

Hu M, Wu BJ, Zhou WB, et al., 2022. Self-driving shield: intelligent systems, methodologies, and practice. *Automation in Construction*, 139:104326. https://doi.org/10.1016/j.autcon.2022.104326

Kannangara KKPM, Ding Z, Zhou WH, 2022. Surface settlements induced by twin tunneling in silty sand. *Underground Space*, 7(1):58-75. https://doi.org/10.1016/j.undsp.2021.05.002

Li Z, Liu XZ, Lai HR, et al., 2023. Detailed damage mechanism of deformed shield tunnel linings reinforced by steel plates. *Engineering Failure Analysis*, 143:106850. https://doi.org/10.1016/j.engfailanal.2022.106850

Li Z, Liu XZ, Yang XL, et al., 2024. Structural damage mechanism and treatment of a shield tunnel under asymmetric unloading. *Tunnelling and Underground Space Technology*, 148:105753. https://doi.org/10.1016/j.tust.2024.105753

Liu DJ, Wang F, Hu QF, et al., 2020. Structural responses and treatments of shield tunnel due to leakage: a case study. *Tunnelling and Underground Space Technology*, 103:103471. https://doi.org/10.1016/j.tust.2020.103471

Liu DJ, Tian C, Zuo JP, et al., 2025. Mechanical behaviour of shield tunnel linings strengthened by steel plates spanning circumferential joints. *Structure and Infrastructure Engineering*, 21(3):459-476. https://doi.org/10.1080/15732479.2023.2211964

Liu TJ, Chen SW, Lin PQ, et al., 2022. Failure mechanism

and strengthening effect of shield tunnel lining reinforced by steel plates with corbels. *European Journal of Environmental and Civil Engineering*, 26(4):1603-1621. https://doi.org/10.1080/19648189.2020.1717636

Liu X, Bai Y, Yuan Y, et al., 2016. Experimental investigation of the ultimate bearing capacity of continuously jointed segmental tunnel linings. *Structure and Infrastructure Engineering*, 12(10):1364-1379. https://doi.org/10.1080/15732479.2015.1117115

Liu X, Dong ZB, Bai Y, et al., 2017. Investigation of the structural effect induced by stagger joints in segmental tunnel linings: first results from full-scale ring tests. *Tunnelling and Underground Space Technology*, 66:1-18. https://doi.org/10.1016/j.tust.2017.03.008

Liu X, Yang ZH, Men YQ, 2021. Temporal variation laws of longitudinal stress on cross section of shield tunnels. *Chinese Journal of Geotechnical Engineering*, 43(1):188-193 (in Chinese). https://doi.org/10.11779/CJGE202101022

Lu CR, Zhang XH, Shi BB, et al., 2024. Deformation in settlement and grouting remediation of thickened larger-diameter metro shield tunnel in soft soil: a case study. *Case Studies in Construction Materials*, 20:e02736. https://doi.org/10.1016/j.cscm.2023.e02736

MOHURD (Ministry of Housing and Urban-Rural Development of the People's Republic of China), 2021. Standard for Design of Shield Tunnel Engineering, GB/T 51438-2021. National Standards of the People's Republic of China (in Chinese).

Ran L, Ding Y, Chen QZ, et al., 2023. Influence of adjacent shield tunneling construction on existing tunnel settlement: field monitoring and intelligent prediction. *Journal of Zhejiang University-SCIENCE A*, 24(12):1106-1119. https://doi.org/10.1631/jzus.A2200573

Sharghi M, Afshin H, Dias D, et al., 2023. 3D numerical study of the joint dislocation and spacing impacts on the damage of tunnel segmental linings. *Structures*, 56:104878. https://doi.org/10.1016/j.istruc.2023.104878

Su D, Chen WJ, Wang XT, et al., 2022. Numerical study on transverse deformation characteristics of shield tunnel subject to local soil loosening. *Underground Space*, 7(1):106-121. https://doi.org/10.1016/j.undsp.2021.07.001

Wang SM, Peng XY, Zhou H, et al., 2023. Deformation control criterion of shield tunnel under lateral relaxation of soft soil. *Frontiers of Structural and Civil Engineering*, 17(5):780-795. https://doi.org/10.1007/s11709-023-0944-3

Wei G, Zhou XX, Xu TB, et al., 2024. Full-scale experimental and structural characterization study of shield tunnel reinforcement under ground stacking loads. *Structures*, 60:105865. https://doi.org/10.1016/j.istruc.2024.105865

Wu HN, Chen S, Chen RP, et al., 2022. Deformation behaviors and failure mechanism of segmental RC lining under unloading condition. *Tunnelling and Underground Space Technology*, 130:104687. https://doi.org/10.1016/j.tust.2022.104687

Wu HN, Liu L, Liu Y, et al., 2023. Weakening behavior of waterproof performance in joints of shield tunnels under adjacent constructions. *Frontiers of Structural and Civil Engineering*, 17(6):884-900. https://doi.org/10.1007/s11709-022-0912-3

Ye XW, Zhang XL, Chen YB, et al., 2024. Prediction of maximum upward displacement of shield tunnel linings during construction using particle swarm optimization-random forest algorithm. *Journal of Zhejiang University-SCIENCE A*, 25(1):1-17. https://doi.org/10.1631/jzus.A2300011

Zhai WZ, Zhang DM, Huang HW, et al., 2023. Numerical investigation into the composite behaviour of over-deformed segmental tunnel linings strengthened by bonding steel plates. *Soils and Foundations*, 63(4):101335. https://doi.org/10.1016/j.sandf.2023.101335

Zheng G, Qiu HM, Zhang TQ, et al., 2024. Experimental study of the effects of contact loss under a shield tunnel invert. *Acta Geotechnica*, 19(6):4189-4199. https://doi.org/10.1007/s11440-023-02157-z

Zhou L, Zhu HH, Shen Y, et al., 2022. Full-scale experimental investigation on progressive failure characteristics of shield segmental lining connected through segmental joints containing ductile-iron joint panels. *Archives of Civil and Mechanical Engineering*, 22(3):120. https://doi.org/10.1007/s43452-022-00438-0